Equilibration of Circumpolar Currents with and without Topography

Ryan Abernathey * and Paola Cessi

Scripps Institution of Oceanography, La Jolla, California

ABSTRACT

The processes that determine the depth of the Southern Ocean thermocline are considered. From the perspective of heat transport, the thermocline depth is determined by the efficiency of the geostrophic circulation at transporting heat poleward. Existing conceptual frameworks focus on the importance of transient eddies, assuming that standing eddies can be neglected through transformation to a "streamwise" coordinate. Using numerical simulations of a simple circumpolar channel, we show that, when topography is present, standing eddies are the primary mechanism of poleward heat transport by the geostrophic circulation. The standing eddies are more efficient at transporting heat than the transient eddies, meaning that a flat-bottomed experiment with identical forcing has a significantly deeper thermocline. The standing eddies are also fundamentally different from transient eddies because they are not adiabatic, i.e. their heat flux is not directed along zonal-mean isotherms but rather has a significant down-gradient component. Analysis of the variance budget shows that this down-gradient transport by standing eddies is in fact sustained by a term related to the transient eddy heat flux. Thus the transient eddies remain important for the equilibration, but play a different role. A simple quasigeostrophic analytical model of a standing eddy is developed which reproduces many characteristics of the numerical solutions. The numerical model is also analyzed in streamwise coordinates; from this viewpoint, the heat balance with topography more resembles the flat-bottomed case, in which transient eddies dominate the geostrophic heat transport across the front. However, unlike the zonally symmetric flat-bottomed case, the transient eddy fluxes are highly localized downstream of topography.

1. Introduction

Mid-latitude gyre flows, confined within closed basins, produce a relatively shallow thermocline. In contrast, the Southern Ocean's unique geometry permits the Antarctic Circumpolar Current (ACC) to circumnavigate the globe, accompanied by much deeper stratification. The deep stratification is necessary for the thermal wind balance of such a strong baroclinic current and is intimately linked to the meridional overturning circulation (MOC). Many studies have shown that the stratification generated in the ACC pervades the global ocean below roughly 500 m depth (Toggweiler and Samuels 1995; **?**; Wolfe and Cessi 2010; Nikurashin and Vallis 2012; Munday et al. 2012). Therefore, to understand the global deep stratification and MOC, it is necessary to understand how the ACC stratification itself is determined and how this equilibrium responds to changes in forcing. There is ample evidence that the wind stress forcing the Southern Ocean has increased over decadal time scales (Marshall 2003; Toggweiler 2009) and may have been drastically reduced during the last glacial maximum (Toggweiler and Russell 2008). The means that the equilibration of the Southern Ocean is an issue of relevance for a wide range of climate problems.

The dominant paradigm for understanding the ACC stratification involves a balance between wind-driven upwelling, which tends to tilt up the isopycnals and deepen the stratification, and transient eddies produced by baroclinic instability, which work to reduce the isopycnal slope (Karsten et al. 2002). These two processes reflect the mean and eddy-driven components of the MOC. Seen from this perspective, the ACC is a version of the classic problem of macroturbulent baroclinic equilibration, similar to the midlatitude atmosphere (Green 1970; Stone 1972; Johnson and Bryden 1989; Schneider 2006; Jansen and Ferrari 2012). An increase in wind-driven upwelling can be partially or completely offset by an increase in eddy-driven restratification, resulting in an insensitivity of the ACC stratification and transport to wind changes; this behavior has been dubbed "eddy saturation" (Straub 1993; Hallberg and Gnanadesikan 2006; **?**; Viebahn and Eden 2010; Farneti et al. 2010; Abernathey et al. 2011; Meredith et al. 2012; Morrison and Hogg 2012; Munday et al. 2012).

In addition to the transient, turbulent eddy field that arises from baroclinic instability, the ACC contains many "standing eddies," steady-state meanders of the current caused by interaction with topographic features such as, for instance, the Kerguelen plateau or the Scotia Arc. There are somewhat conflicting views regarding the importance of

standing eddies in the Southern Ocean. On one hand, when the zonally-averaged fluxes due to transient and standing eddies are decomposed separately, it is clear that the standing component dominates in both idealized models with simple topography (**????**) and in realistic eddy-permitting models (Marshall et al. 1993; Karoly et al. 1997; Olbers and Ivchenko 2001; Lee and Coward 2003; **?**; **?**; Dufour et al. 2012). Inspired by the observation of de Szoeke and Levine (1981) that the mean geostrophic flow of the ACC does not transport heat across a contour of depth-averaged temperature, many authors have advocated thinking about the ACC in a "streamwise" coordinate, in order to remove the standing eddy component and emphasize importance of transient eddies (Marshall et al. 1993; Olbers et al. 2004). This streamwise-averaged perspective underpins the contemporary theoretical model of the ACC (Marshall and Radko 2003; Olbers and Visbeck 2005). Neverthless, in practice, many of the latest models continue to be analyzed using a simple zonal average (Hallberg and Gnanadesikan 2006; **?**; **?**; **?**; **?**; **?**; **?**; **?**; **?**), rather than a streamwise average, leading to a profound disconnect with the theory. (Notable exceptions are **?** and Viebahn and Eden (2012).) It is striking that even the original proponents of the streamwise coordinate (Marshall et al. 1993) declined to analyze their numerical results in this framework due to the practical difficulty, opting instead for a standard zonal average. As a result, the role of standing eddies in the eddy saturation phenomenon remains unclear.

Our study seeks to gauge the importance of standing eddies by comparing the equilibration of model ACCs with and without topography, focusing on the thermocline depth at the northern boundary as a metric of stratification. Our simulations clearly show that, in the the presence of the ridge, the stratification is significantly shallower. The thermocline always remains well above the ridge crest, so this is not a direct effect of the intrusion of topography, but rather a result of the strong southward heat transport by the standing wave. Furthermore, the stratification in the channel with a ridge displays even weaker sensitivity to wind changes; the saturation is more complete. This indicates that standing eddies are more efficient at restratifying the channel than transient eddies alone.

The time-mean flow in the ridge experiment is characterized by a large scale meander which we call the "standing wave." We perform detailed diagnostics of this standing wave, which reveal several interesting aspects. The standing wave heat flux is far from adiabatic—it has a strong component across the zonal-mean isotherms, in contrast to the transient eddy heat flux in the flat-bottomed case. To explain this behavior, we derive a temperature variance budget for the standing wave. This budget includes a term proportional to the transient-eddy heat flux convergence, which turns out to be the dominant driver of the meridional heat transport by the standing wave. We develop a quasi-linear analytical model for the standing wave that parameterizes this term as a simple Rayleigh damping of the wave temperature anomaly. Despite many simplifications, this model shows good qualitative agreement with the numerical solutions and provides valuable insight into the standing-wave dynamics.

As a final step, we analyze the heat budget in streamwise coordinates. We use two different definitions of the streamwise coordinate: the depth-integrated temperature and the barotropic transport streamfunction. The results are the same in both cases: the standing eddy flux across these contours nearly vanishes, and the transient eddies instead dominate the heat transport by the geostrophic flow. However, in contrast the the flat-bottomed case, the transient eddy heat fluxes are highly localized downstream of the topography, in a region of high eddy energy and strong gradients. This results in an overall more efficient cross-stream heat transport by the transient eddies compared with the flat-bottomed case. By diagnosing a local eddy efficiency parameter (related to an eddy diffusivity), we highlight the importance of the high-mixing region downstream of the ridge.

Throughout the paper, we frame our discussion in terms of meridional heat transport. But we note that the meridional heat transport is directly related to the vertical flux of momentum by eddies, i.e. the interfacial form stress, which is so important for the momentum balance of the ACC (Johnson and Bryden 1989; Marshall et al. 1993; Hughes 1997; Olbers 1998). One advantage of working with heat transport is that is can be integrated vertically, allowing us to easily compare the contributions of different parts of the flow. But our results regarding the relative importance of standing and transient eddies in the heat balance carry over to the momentum balance as well. *[[Here would be a good place for a discussion of Matt Mazzloff's new paper, in which standing eddies in the surface layer support a mean pressure gradient that is very important in the momentum balance.]]*

Our paper is organized as follows. Section 2 describes the model setup and experiment design. Section 3 defines a framework for characterizing the efficiency of restratification by standing and transient eddies and then applies this framework to diagnose the simulations. Section 4 contains the detailed diagnostics of the standing wave in a reference simulation. In Section 5, we present the quasi-linear analytical model of the standing wave. Analysis of the heat transport in streamwise coordiantes is conained in Section 6. Finally, discussion of the results and conclusions are given in Section 7.

2. Numerical Model Experiments

The goal of our study is investigate the relative importance of transient and standing eddies in a simple way in

order to reveal the underlying physics. The key ingredients of our model are (1) a zonally-reentrant domain, which allows a zonal current to develop; (2) westerly wind stress forcing, which drives an Eulerian-mean overturning; (3) surface buoyancy restoring, which maintains a meridional buoyancy gradient; and (4) a topographic obstruction in the abyss. We work in the adiabatic regime, with interior diapycnal mixing as weak as numerics will permit, and we use a linear equation of state with no salinity. While this setup is highly idealized, the relatively fine resolution (5 km) resolves the mesoscale eddy field well.

Following Marshall and Radko (2003), our assumption is that the first-order buoyancy balance in the ACC is between wind-driven advection by the Ekman circulation and eddy-induced advection, and that this balance determines the stratification. A second-order balance exists between the residual overturning circulation and diabatic processes, such as air-sea exchange, interior diapycnal mixing, and exchange with basins to the north. By supressing diapycnal mixing and not representing the connection to other basins, our model ACC approaches the limit of zero residual circulation described by Johnson and Bryden (1989) or Kuo et al. (2005). This means our model is appropriate for studying the first-order problem of the stratification, but not the second-order problem of the residual circulation.

The model grid and numerical parameters are nearly identical to those described in Abernathey et al. (2011), to which the reader is referred for further details. The code solves the hydrostatic, primitive, Boussinesq equations in Cartesian coordinates using the MITgcm (Marshall et al. 1997a,b). The domain is a box $L_x = 2000$ km x $L_y = 2000$ km x $H = 2985$ m. The wind stress forcing is a zonally-symmetric sinusoidal westerly jet of maximum strength τ_0 in the center of the domain, such that $\tau = \tau_0 \sin(\pi y/L_y)$. For the reference simulations, $\tau_0 = 0.2$ N m^{-2}.

The model's potential temperature equation can be written as

$$\theta_t + \boldsymbol{u} \cdot \nabla\theta = \kappa_h \nabla_h^2 \theta + (\kappa_v \theta_z)_z - \frac{\lambda}{\delta}(\theta_s - \theta^*) \ . \quad (1)$$

Here κ_h is a spatially uniform horizontal diffusivity and κ_v is a vertical diffusivity. Advection is performed using a second-order-moment scheme (Prather 1986). Explicit diffusivity (κ_h and κ_v) is set to zero, and a detailed analysis has shown that the effective numerical diapycnal diffusivity in this model is weaker than 10^{-5} m^2 s^{-1}, meaning the interior is highly adiabatic (Hill et al. 2012). However, the KPP scheme (Large et al. 1994) is employed to simulate the surface mixed layer, where κ_v is greatly enhanced. The final term represents the surface forcing, active only in the top model level; λ is a temperature relaxation inverse timescale, and δ is the thickness of the top grid cell. The surface temperature θ_s is relaxed to a linear function of latitude of the form $\theta^* = \Delta\theta(y/L_y)$. The minimum temperature is 0°C, and we choose a maximum temperature $\Delta\theta = 8$°C. This leads to a maximum buoyancy contrast of $\Delta b = g\alpha\Delta T = 1.6 \times 10^{-2}$ m s^{-2}. The relaxation timescale λ^{-1} is chosen to be 30 days (Haney 1971), which keeps the actual surface temperature very close to the prescribed profile.

In simulations with topography, a gaussian-shaped ridge is present in the middle of the domain. The motivation for this form was to capture the large meridional obstructions encountered by the ACC along is path, such as Kerguelen Plateau or the Scotia Arc. The depth in this case is given by

$$-H + h_0 e^{-x^2/\sigma^2} \ . \quad (2)$$

We selected $h_0 = 1000$ m, about one third of the total depth, and $\sigma = 75$ km, leading to a steep ridge. However, the topographic length scale σ is still large compared to the deformation radius which is approx. 15 km in the middle of the domain. Different topographic geometries can lead to different types of standing waves (**?**), but we did not explore other forms, focusing instead on the gross differences with and without topography.

The model equilibrates after about 100 years of spinup. Snapshots of the temperature field from the equilibrated state are show in Fig. 1. The time-mean isotherms are also superimposed. While both simulations contain mesoscale eddies, the figure illustrates how the flat-bottomed case is statistically symmetric in x, while the ridge case contains a standing wave in the time-mean $\overline{\theta}$ field.

3. Eddy Saturation and the Meridional Heat Transport

The mean meridional heat transport (MHT) across a latitude circle is given, in the Boussinesq approximation, by

$$\mathcal{H} = \rho_0 c_p L_x \int_{-H}^{0} \langle v(\theta - \theta_0) \rangle dz \quad (3)$$

where ρ_0 and c_p are, respectively, the reference density and specific heat of seawater, v is the meridional velocity, θ is the potential temperature, and the angle brackets indicate a zonal and time average (**?**). Since the total vertically-integrated mass flux across a latitude circle (or any other circumpolar contour) must vanish, an arbitrary constant θ_0 can be chosen without changing $\mathcal{H}$ (de Szoeke and Levine 1981). By choosing this constant to be the temperature of the abyss, 0° C, we can allow ourselves to ignore the contribution to the heat transport by the deep mean flows, such as the bottom Ekman flow or the geostrophic flow below topography, in which $\theta \simeq \theta_0$.

In the adiabatic limit, $\mathcal{H}$ must tend to zero in a model such as ours. This is because any nonzero $\mathcal{H}$ must be balanced by an air-sea heat flux, which also tends to zero. This is most obvious from the perspective of water-mass transformation (**?**). In a closed basin, the lack of interior

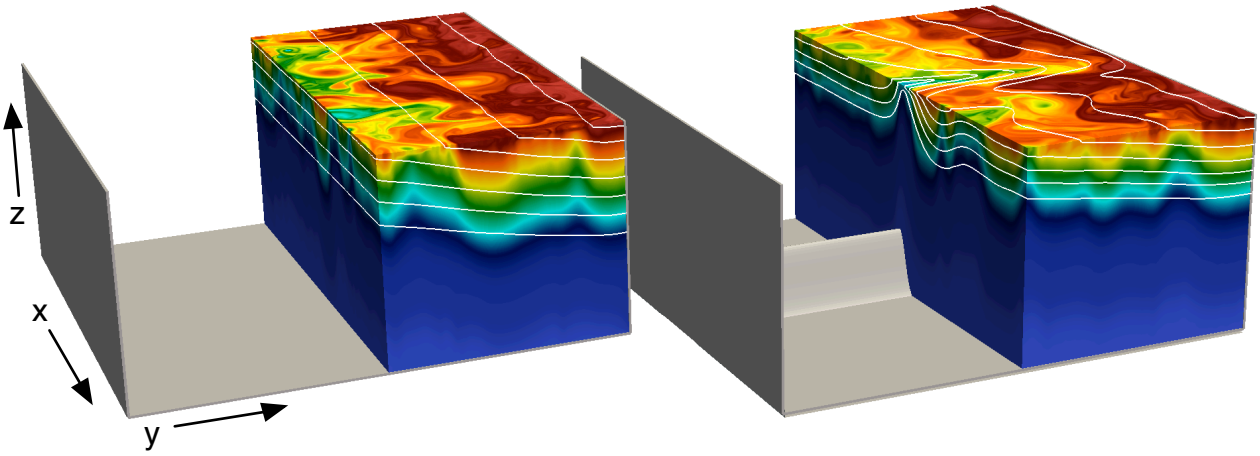

FIG. 1. Colors show an instantaneous snapshot of the θ field from each reference experiment (flat on the left, ridge on the right). The color scale ranges from 0 to 8°C. The field has been clipped at $y = 1000$ km, the meridional midpoint, to reveal a zonal cross section. The white contours are the time-mean isotherms $\overline{\theta}$, illustrating the statistical zonal symmetry of the flat-bottomed case and the standing wave in the ridge.

transformation by diapycnal mixing implies that the air-sea heat flux must also vanish; otherwise water mass formation at the surface would continuously add or remove volume from density classes, and a steady state would be impossible to reach (**?**). Without an air-sea heat flux, there can be no MHT or residual MOC (Marshall and Radko 2003). In practice, we do not achieve a truly vanishing MOC or MHT due to diabatic effects in the surface layer. Our model contains a weak overturning cell in the top 200 m, similar to the one noted by Kuo et al. (2005). However, this is clearly a second-order effect, and as the subsequent analysis shows, we remain very close to the limit of zero net MHT. This vanishing-residual MOC limit is a useful idealization of the real ACC, in which there is a nonzero MHT and MOC, but where large cancellations between mean and eddies nevertheless occur (Speer et al. 2000; Hallberg and Gnanadesikan 2006; **?**).

We can use this constraint on the heat transport to derive a scaling for the termocline depth. We divide the heat transport into a part due to the ageostrophic motion, $\mathcal{H}_{Ek}$, and a part due to the gostrophic motions, $\mathcal{H}_g$ due to eddies and waves. Thanks to our choice of θ_0, $\mathcal{H}_{Ek}$ is simply the heat transported in the Ekman layer:

$$\mathcal{H}_{Ek} = \rho_0 c_p L_x V_{Ek} \langle \theta_s \rangle \sim -c_p L_x \frac{\tau}{f} \Delta\theta \frac{y}{L_y} \,, \tag{4}$$

which is an equatorward heat transport determined solely by externally specified parameters.

We also have the heat transport by the geostrophic flow:

$$\mathcal{H}_g = \rho_0 c_p L_x \int_{-H}^{0} \langle v_g \theta \rangle dz \sim \rho_0 c_p L_x h \widetilde{v_g \theta} \,, \tag{5}$$

where $\widetilde{v_g\theta}$ represents the typical value of the geostrophic transport due to eddies and waves in the thermocline.

As illustrated in figure 2, $\mathcal{H}_g$ occurs over the thermocline of depth h. Because there is no net zonal pressure gradient above the topography, $\langle v_g \rangle = 0$, meaning that $\mathcal{H}_g$ arises only from eddy correlations; it potentially contains contributions from both standing and transient eddies. When topography is present, there can be a deep geostrophic mean flow. However, because of our choice of θ_0, this does not contribute to $\mathcal{H}_g$. As a practical definition, we take the vertically-averaged geostrophic heat transport within the thermocline to be

$$\widetilde{v_g\theta}(y) = h^{-1} \int_{-h}^{0} \langle v_g \theta \rangle dz \,. \tag{6}$$

For our geometry the total heat transport almost vanishes, i.e. $\mathcal{H} = \mathcal{H}_{Ek} + \mathcal{H}_g \approx 0$, and this leads to a scaling of the thermocline depth given by

$$h \sim \frac{\tau_0 \Delta\theta}{\rho_0 |f| L_y \widetilde{v_g\theta}} \,. \tag{7}$$

The scaling for h is not completely satisfactory since it depends on the unknown geostrophic heat transport due to eddy and waves, but is serves as a useful measure of the efficiency of the geostrophic motion in stratifying the fluid against the overturn due to the Ekman cell. If the efficiency of the eddies does not change with the winds, $\widetilde{v_g\theta}$ will remain constant and the thermocline depth will scale linearly with depth.The concept of "eddy saturation," in which h becomes independent of τ_0, implies that $\widetilde{v_g\theta} \propto \tau_0$. In general $\widetilde{v_g\theta}$ exhibits a dependence on τ_0 that is

intermediate between these two limits (Spence et al. 2009; Meredith et al. 2012). Here we contrast the sensitivity of $\widetilde{v_g\theta}$ and h to τ_0 with and without topography, finding a higher level of saturation, i.e. a smaller dependence of h on the wind stress, when topography is present. In section ??? we argue that eddies are simply more efficient when the ridge is present.

As a practical matter, we find h via the expression

$$h = 2\frac{\int_{-H}^{0} z\langle\theta\rangle dz}{\int_{-H}^{0}\langle\theta\rangle dz} \tag{8}$$

evaluated at the northern boundary, where the thermocline is deepest. This is a standard method for characterizing thermocline depth (**???**).

To illustrate these concepts, we present diagnostics of $\langle v_g\theta\rangle$ and $\mathcal{H}$ in Fig. 2. This figure compares the reference simulations ($\tau_0 = 0.2$ N m^{-2}) with and without the topographic ridge. The upper panel demonstrates that $\mathcal{H}_{Ek}$ and $\mathcal{H}_g$ are essentially the same in both cases, with $\mathcal{H}_{Ek}$ remaining very close to the approximation defined in (4). $\mathcal{H}_g$ compensates almost completely for $\mathcal{H}_{Ek}$, meaning that $\mathcal{H}$, the net MHT, remains very close to zero. The difference between the two simulations is only revealed when the bottom panel is examined; the heat transport in the ridge case is confined to a shallower layer, implying a smaller value of h, i.e. a shallower thermocline. Specifically, according to (8), the thermocline depth at the northern boundary is approx. 1200 m in the flat-bottom experiment and 1000 m in the ridge experiment. While this difference might seem small, this difference increases as the wind-stress increases. Figure 3 (top-left panel) shows the thermocline depth as a function of wind stress, for both the flat and ridge experiments, for the following values of τ_0: 0.0125, 0.025, 0.05, 0.1, 0.2, 0.4, and 0.8 N m^{-2}. This range constitutes six successive doublings of the wind stress. It is clear that the dependence of h with τ_0 is much weaker in the ridge case. The general principle of eddy saturation is reflected in h: as the winds increase, the geostrophic flow becomes more and more efficient at transporting heat poleward, leading to a weak dependence of h on τ_0.

The difference of dependence of h on τ_0 is amplified in the zonal baroclinic transport[1], given by

$$T = -\frac{g\alpha}{f}\int_0^{Ly}\int_{-2000\text{ m}}^{0}\frac{\partial\langle\theta\rangle}{\partial y}dzdy\ . \tag{9}$$

Because $\langle\theta\rangle_y$ remains fixed at the surface, $T \propto h^2$. If the total zonal transport were considered, the difference between the flat and ridge cases would be even larger because, in addition to T, the total transport also includes a susbtantial barotropic component, which is frictionally balanced in the absence of topography (**?**Cessi 2007; Abernathey et al. 2011) and thus very large for small bottom drag. In the ridge case, this frictional component is mostly absent, and the bottom velocity is determined through the topographic form drag available to close the zonal momentum budget (**?**), leading to much smaller values of the bottom flow. To illustrate this difference we show in figure 3 the zonally averaged bottom zonal velocity averaged over the center half of the channel, as a function of τ_0, with and without the ridge: with the ridge the bottom velocity is one order of magnitude smaller, and largely independent of the bottom drag. The net result is that the zonally averaged zonal flow is much smaller when the ridge is present throughout the water column.

Recent studies have used the domain-averaged transient eddy kinetic energy (EKE) as a proxy for the strength of the eddy-driven circulation (Meredith and Hogg 2006; Abernathey et al. 2011; Meredith et al. 2012; **?**; Munday et al. 2012). According to this argument, a model with a higher EKE will have a higher $\widetilde{v_g\theta}$ and therefore a shallower thermocline. To test this idea, we calculated the EKE in our simulations (Fig. 3). Both models have very similar EKE for weak values of τ_0. As the winds are increased, the values diverge; the EKE in the flat-bottomed model is always *higher* than the corresponding ridge case and is nearly linearly proportional to τ_0. The EKE in the model with topography displays a slightly weaker dependence on τ_0. Nevertheless, $\widetilde{v_g\theta}$ is greater with topography. This seems to upset the paradigm put forth by Meredith et al. (2012), in which the EKE dependence on winds controls the degree of eddy saturation.

This simple set of experiments demonstrates the importance of topographic effects in determining the Southern Ocean stratification. No coordinate transformation (e.g. to a streamwise coordinate system) will alter the fact that the stratification at the northern boundary is shallower when topography is present, or that the thermal-wind zonal transport and the total zonal transport are much less. But beyond these quantitative differences, there are great qualitative differences in how the two system equilibrate. In the rest of the paper, we further explore the results from two different perspectives. From the standard zonally-averaged perspective, the clear difference is that topography generates a standing wave which is highly efficient at transporting heat poleward. In the next section, we diagnose the model from this perspective. We decompose $\mathcal{H}_g$ into transient and standing components and show that the standing component becomes increasingly dominant as the winds increase. In Sec. 6, we instead consider the "streamwise" perspective, in which standing eddy fluxes are greatly reduced. From this perspective, a highly localized region of cross-stream transient eddy heat flux downstream of the ridge is responsible for the greater overall heat transport efficiency. While both these perspectives are formally "correct," they

[1]We integrate only above 2000 m, the depth of the ridge crest, to fairly compare both experiments.

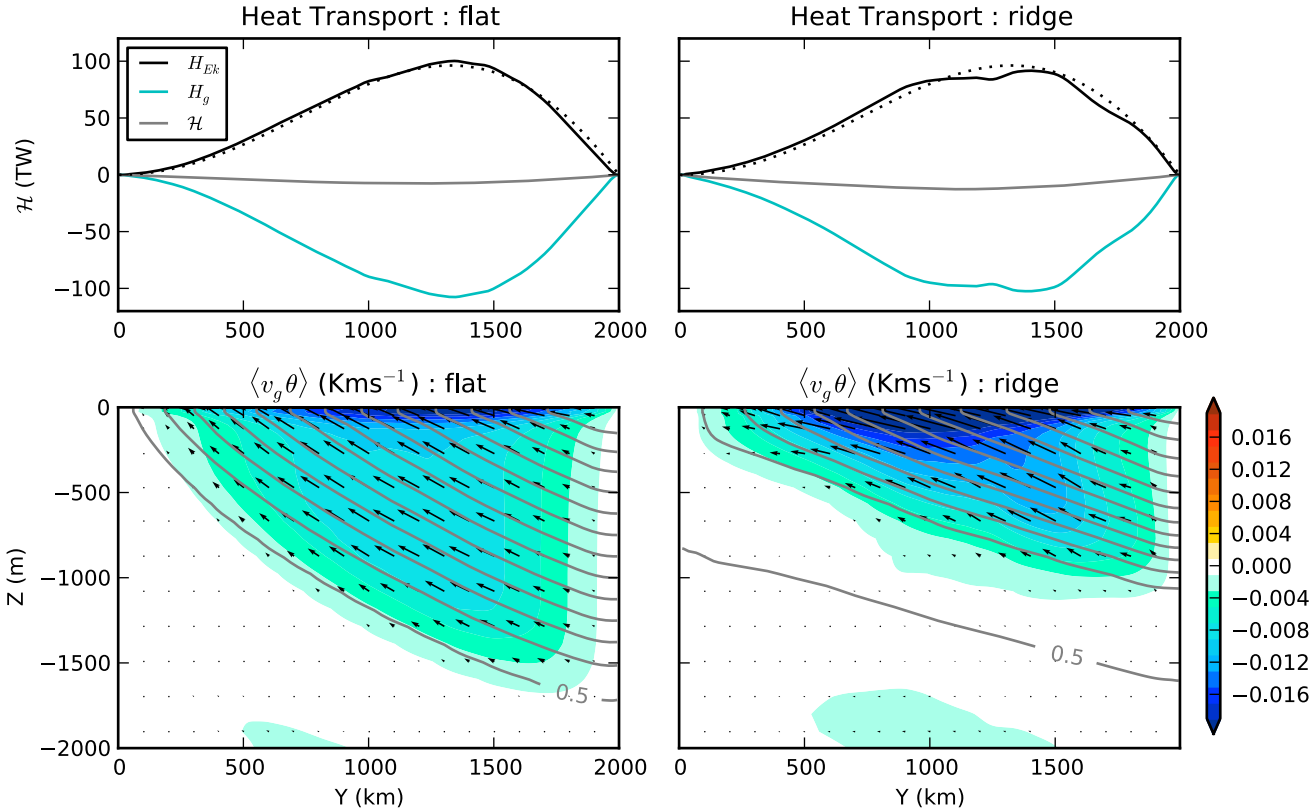

FIG. 2. *Top panel:* the meridional heat transport, $\mathcal{H} = \mathcal{H}_{Ek} + \mathcal{H}_g$, from the reference experiments. The black dotted line is the approximate form of $\mathcal{H}_{Ek}$ from the RHS of (4). $\mathcal{H}_g$ is just the vertical integral of the bottom panel. *Bottom panel:* zonal and time-mean temperature flux by the geostrophic flow $\langle v_g\theta\rangle$ in color. The black arrows indicate the direction the flux in the (y, z) plane and the grey contours show the zonal mean isotherms $\langle\theta\rangle$, contoured every $0.5°C$. Only the top 2000 m are plotted; below there is no significant heat flux or stratification.

offer complementary views on the dynamics responsible for equilibrating the thermocline.

4. Heat Transport by the Standing Wave

a. Standing and Transient Eddies

At this point, we must carefully define conventions for time and zonal averaging. The time average of a variable $A(x, y, z, t)$ over interval ΔT is

$$\overline{A}(x, y, z) = \Delta T^{-1} \int_t^{t+\Delta T} A dt \ . \tag{10}$$

We will only take zonal averages of already time-averaged fields. Other conventions are possible (see discussion in Viebahn and Eden 2012), but this is the most informative decomposition. The zonal / time average is

$$\langle A\rangle(y, z) = \langle\overline{A}\rangle = L_x^{-1} \int_0^{L_x} \overline{A} dx \ . \tag{11}$$

We define the anomalies as follows:

$$\begin{aligned} A' &= A - \overline{A} \\ A^\dagger &= \overline{A} - \langle A\rangle \end{aligned} \tag{12}$$

such that $A = \langle A\rangle(y, z) + A^\dagger(x, y, z) + A'(x, y, z, t)$. The standing wave is associated with $A^\dagger$. In a flat-bottom simulation with statistical symmetry in the x direction, $A^\dagger = 0$.

Taking a zonal and time average of the θ equation (1), we obtain

$$\begin{aligned} \langle \boldsymbol{u}\rangle \cdot \nabla\langle\theta\rangle + \nabla \cdot \langle \boldsymbol{u}^\dagger\theta^\dagger\rangle + \nabla \cdot \langle\overline{\boldsymbol{u}'\theta'}\rangle = \\ \kappa_h \nabla_h^2\langle\theta\rangle + (\langle\kappa_v\theta_z\rangle)_z - \frac{\lambda}{\delta}(\langle\theta\rangle_0 - \theta^*) \ . \end{aligned} \tag{13}$$

Integrating this equation once in y gives an equation for the meridional heat transport. All the diabatic terms on the RHS are quite small compared to the advective terms. To relate these advective terms to the components of the heat transport mentioned in the previous section, we note

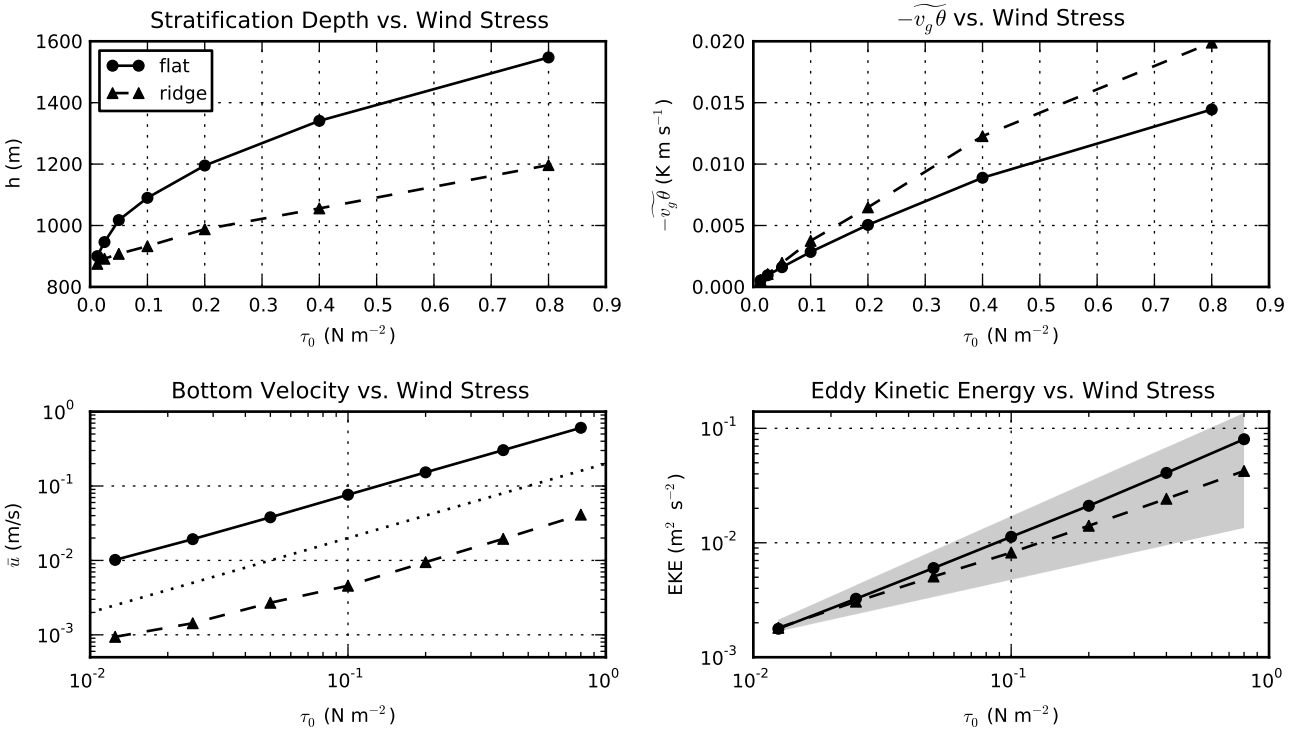

FIG. 3. Comparison of global variables in flat-bottom (circles, solid lines) and ridge (triangles, dashed lines) experiments. *Top left:* the stratification depth h at the northern boundary, evaluated from (8). *Top right:* The magnitude of the meridional heat transport within the thermocline by the geostrophic flow, $\widetilde{v_g\theta}$, averaged meridionally over the northern half of the domain. *Bottom left:* The zonal mean zonal flow at the bottom, averaged over the center third of the domain, plotted in log-log space. *Bottom right:* the eddy kinetic energy, plotted in log-log space. The gray envelope indicates the range of proportionality between $\tau_0^{1/2}$ and τ_0^1.

that $\langle v \rangle$ is associated with the Ekman overturning, and therefore

$$\mathcal{H}_{Ek} = \rho_0 c_p L_x \int_{-H}^{0} \langle v \rangle \langle \theta \rangle dz \tag{14}$$

while $\mathcal{H}_g$ can be split into two components, one due to standing eddies ($\mathcal{H}_{SE}$) and another due to transient eddies ($\mathcal{H}_{SE}$) :

$$\begin{aligned} \mathcal{H}_g &= \rho_0 c_p L_x \int_{-H}^{0} (\langle v^\dagger \theta^\dagger \rangle + \langle \overline{v'\theta'} \rangle) dz \\ &= \mathcal{H}_{SE} + \mathcal{H}_{TE} \ . \end{aligned} \tag{15}$$

For the flat-bottom experiments, $\mathcal{H}_{SE} = 0$.

In Fig. 4, we use this framework to decompose $\mathcal{H}_g$ from Fig. 2 into standing and transient eddy contributions. This figure makes it clear that $\mathcal{H}_{SE}$ is the dominant contributor. This result has been found whenever eddy fluxes are decomposed in this way, in a wide range of models (**????**Olbers and Ivchenko 2001; Lee and Coward 2003; **?**; **?**; Dufour et al. 2012). Nevertheless, we point it out again here because the recent literature has focused so much on the importance of *transient* eddies in eddy saturation and compensation (**??**Meredith et al. 2012; Morrison and Hogg 2012).

Fig. 4 illustrates the balance in a single experiment but does not address the response to changing winds. We now plot the $\mathcal{H}_g$, $\mathcal{H}_{SE}$ and $\mathcal{H}_{TE}$ at $y = 1250$ km (approximately where the heat transport is most intense) as a function of τ_0 for each of the experiments in Fig. 5. The figure shows that it is $\mathcal{H}_{SE}$ which responds to compensate for the increasing value of $\mathcal{H}_{Ek}$. In fact, $\mathcal{H}_{TE}$ actually *decreases* weakly with τ_0 at this latitude, becoming more and more negligible in comparison with $\mathcal{H}_{SE}$. We conclude that, when analyzed from a zonally averaged perspective, the eddy saturation is primarily a phenomenon of *standing* eddy saturation. A similar conclusion was recently reached by Dufour et al. (2012) in the analysis of the overturning circulation of a realistic Southern Ocean model.

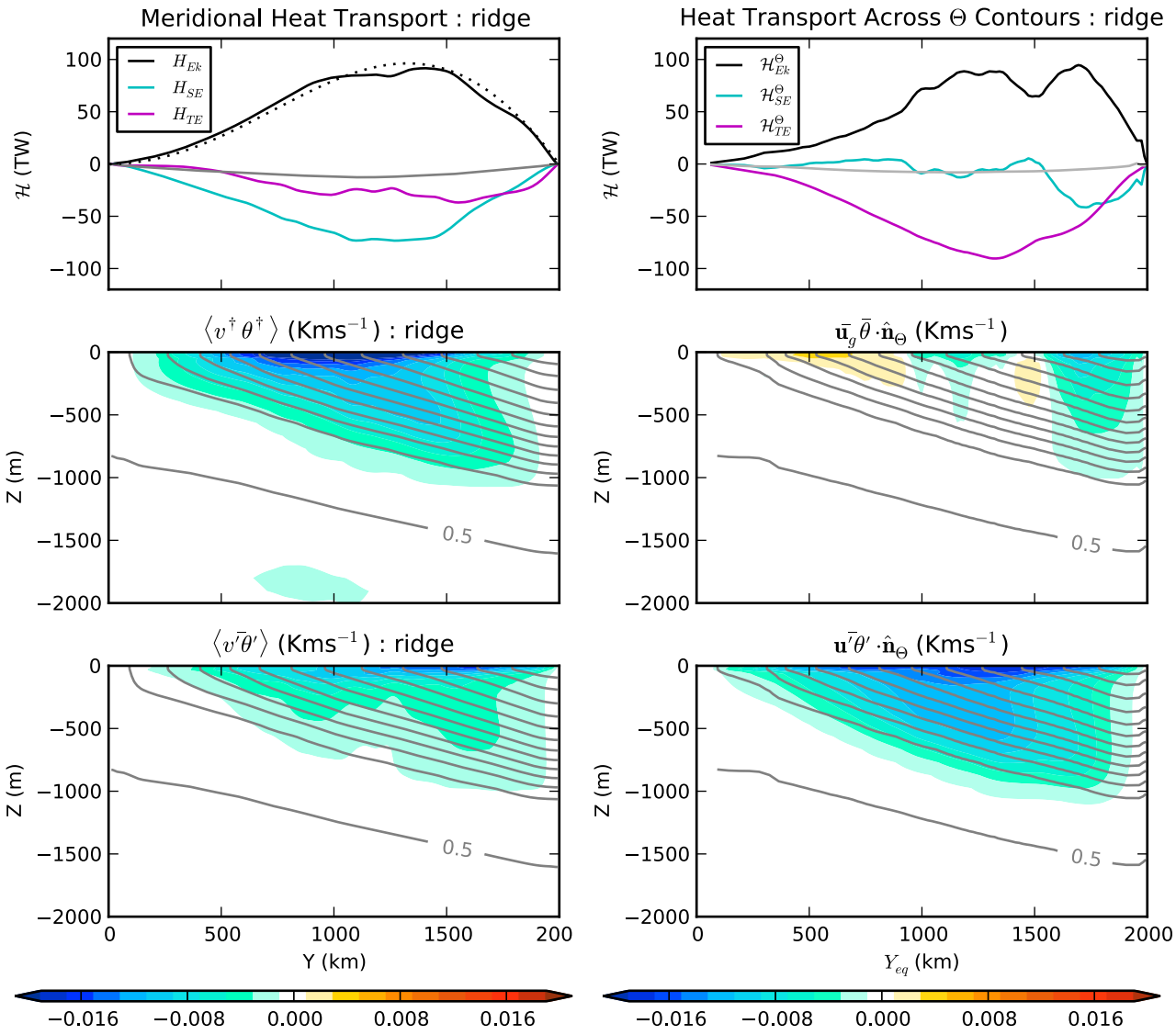

FIG. 4. *Top left:* the meridional heat transport from the ridge experiment, with $\mathcal{H}_g$ decomposed into standing ($\mathcal{H}_{SE}$) and transient ($\mathcal{H}_{TE}$) eddy components. Otherwise the same as Fig. 2. *Middle left:* The standing eddy meridional flux $\langle v^{\dagger}\theta^{\dagger}\rangle$, which integrates vertically to H_{SE}. *Bottom left:* The transient eddy meridional flux $\langle v^{\dagger}\theta^{\dagger}\rangle$, which integrates vertically to H_{SE}. *Top right:* Components of the heat transport across Θ-contours, as a function of Y_{eq}, the equivalent latitude. *Middle right:* The flux across Θ-contours by the steady geostrophic flow. *Bottom right:* The flux across Θ-contours by the transient eddies.

b. What drives the standing eddy heat transport?

It is clear why transient eddies must transport heat toward the pole in the flat-bottom case. Arising from baroclinic instability of the mean state, their energy source is the available potential energy (APE) contained in the sloping isopycnals of the ACC. The transfer from APE to EKE is expressed in the eddy energy budget as a positive term $g\alpha\langle\overline{w'\theta'}\rangle$. Under statistically steady, adiabatic conditions, this vertical heat flux must be accompanied by a meridional flux $-\langle\overline{v'\theta'}\rangle\langle\theta\rangle_y = \langle\overline{w'\theta'}\rangle\langle\theta\rangle_z$, so that the heat flux is directed entirely *parallel* to the mean isotherms, with no cross-gradient component. This behavior is evident in Fig. 2 (left panel), which includes arrows showing the direction of the heat flux in the meridional plane; the arrows clearly point along the isotherms. Because of this energy pathway, when transient eddies are the only contributor to

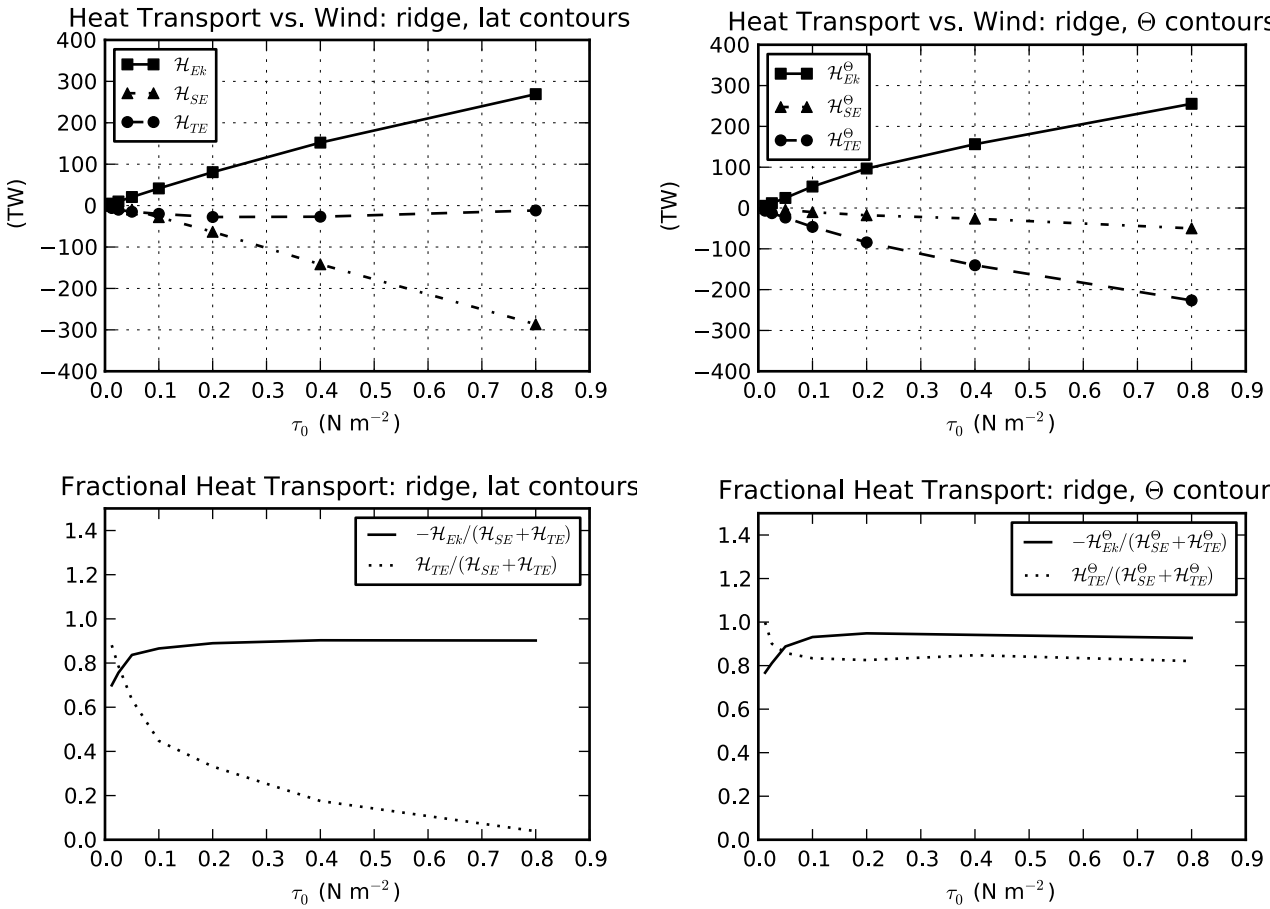

FIG. 5. Dependence of heat transport components on τ_0, the wind stress magnitude. To obtain mean values for each experiment, each component from Fig. 4 was averaged meridionally over the northern half of the domain. On the left are components of the meridional heat transport, i.e. transport across latitude circles. On the right are components of the transport across Θ-contours. The top panels show the raw values, while the bottom panels show ratios.

the MHT, it is indeed reasonable to associate increased $\mathcal{H}_g$ with higher EKE.

It is not so obvious why standing eddies should transport heat poleward. They do not arise from baroclinic instability, but rather from a dynamically complex interaction of the current with topography. The meanders of the ACC are often explained using an "equivalent barotropic" analysis, in which the current is characterized by a single mode which decays (usually exponentially) with depth (**?**). While such models successfully explain many of the features of the ACC, they says nothing about the heat transport by standing eddies. This is because equivalent barotropic flow cannot transport any heat. Heat transport in geostrophic flow requires at least two vertical modes (**?**).

Some progress can be made by considering the standing-wave variance budget. To derive this budget, subtract (13) from (1), multiply the result by $\theta^\dagger$, and take a zonal and time average. The result,

$$\frac{\partial}{\partial t}\frac{\langle\theta^{\dagger 2}\rangle}{2} + \nabla\cdot\left(\langle\boldsymbol{u}\rangle\frac{\langle\theta^{\dagger 2}\rangle}{2} + \frac{\langle\boldsymbol{u}^\dagger\theta^{\dagger 2}\rangle}{2}\right) + \langle\boldsymbol{u}^\dagger\theta^\dagger\rangle\cdot\nabla\langle\theta\rangle = -\langle\theta^\dagger\nabla\cdot(\overline{\boldsymbol{u}'\theta'})\rangle - \text{diabatic terms}\ , \tag{16}$$

where the diabatic terms include terms dependent on diffusivity κ and air-sea damping λ. This equation resembles a standard tracer variance equation, except for the first term on the RHS, which describes the interaction of the standing eddies with the transient eddies.

We have diagnosed this budget from our simulations. The diabatic terms are negligible except for a small contribution close to the surface. This indicates that surface forcing is not important for driving the standing-wave heat

transport. The mean advection term is also small. If we neglect these terms, we can rearrange the equation in a way that reveals how the standing-wave meridional heat transport can be supported:

$$\langle v^\dagger\theta^\dagger\rangle\langle\theta\rangle_y \simeq -\langle w^\dagger\theta^\dagger\rangle\langle\theta\rangle_z - \nabla\cdot\frac{\langle \boldsymbol{u}^\dagger\theta^{\dagger 2}\rangle}{2} - \langle\theta^\dagger\nabla\cdot(\overline{\boldsymbol{u}'\theta'})\rangle \quad (17)$$

The three terms on the right each represent a distinct physical process driving the standing eddy heat transport. The first is associated with the vertical buoyancy flux by the standing wave. The second is the so-called nonlinear "triple correlation" term, resulting from advection of $\theta^{\dagger 2}$ by the standing wave itself. The final one is due to the correlation of $\theta^\dagger$ with heat flux convergence by the transient eddies. The vertical averages of the terms in (17) are plotted in Fig. 6.

Overall the balance can be summarized as follows. All terms are significant in some part of the domain. However, there is a large degree of cancellation between the vertical flux term and the triple correlation term. On the other hand, the transient-eddy term is clearly the dominant driver of the poleward heat transport by the standing wave. Standing wave variance is primarily created by the $\langle v^\dagger\theta^\dagger\rangle\langle theta\rangle_y$ term and destroyed by the $\langle\theta^\dagger\nabla\cdot(\overline{\boldsymbol{u}'\theta'})\rangle$ term. This is an interesting result; it means that, although the transient eddies are relatively unimportant in the meridional heat transport itself, the local transient eddy heat convergence can nevertheless be crucial for maintaining the standing wave meridional heat transport.

This conversion term reappears in the transient eddy variance budget, which we write approximately as

$$\overline{v'\theta'}\langle\theta\rangle_y \simeq -\overline{w'\theta'}\langle\theta\rangle_z + \langle\theta^\dagger\nabla\cdot(\overline{\boldsymbol{u}'\theta'})\rangle\ . \quad (18)$$

Triple correlation terms have been neglected because they are smaller in the case of transient eddies. The vertical average of this balance is also plotted in Fig. 6. Here we see that the conversion term is a strong *source* of transient eddy variance, in addition to the term $\overline{v'\theta'}\langle\theta\rangle_y$. As a result, the vertical transient eddy flux term $\overline{w'\theta'}$ must work overtime to destroy transient eddy variance. Energetically, this destruction acts as a *source* of transient eddy kinetic energy. Most of the dissipation therefore occurs on the transient eddy kinetic energy, primarily through bottom drag.

(**?**) recently examined the changes in overturning a realistic eddying model of the Southern Ocean in terms of both latitude-density coordinates (the conventional framework for diagnosing the MOC) and also an innovative density-depth coordinate system. In the conventional framework, they found that changes in Ekman fluxes were primarily compensated by changes in standing eddy fluxes, as we also found here. But in the density-depth coordinate, where the vertical flux rather than meridional flux plays the primary role, the compensation was between Ekman fluxes and transient eddy fluxes, with standing eddies playing a much smaller role. This is entirely consistent with our analysis of the variance budget, which helps explain why vertical fluxes due to transient eddies must remain high even when transient eddies do not contribute strongly to the variance budget. These transient-eddy vertical buoyancy fluxes are the main path to energy dissipation.

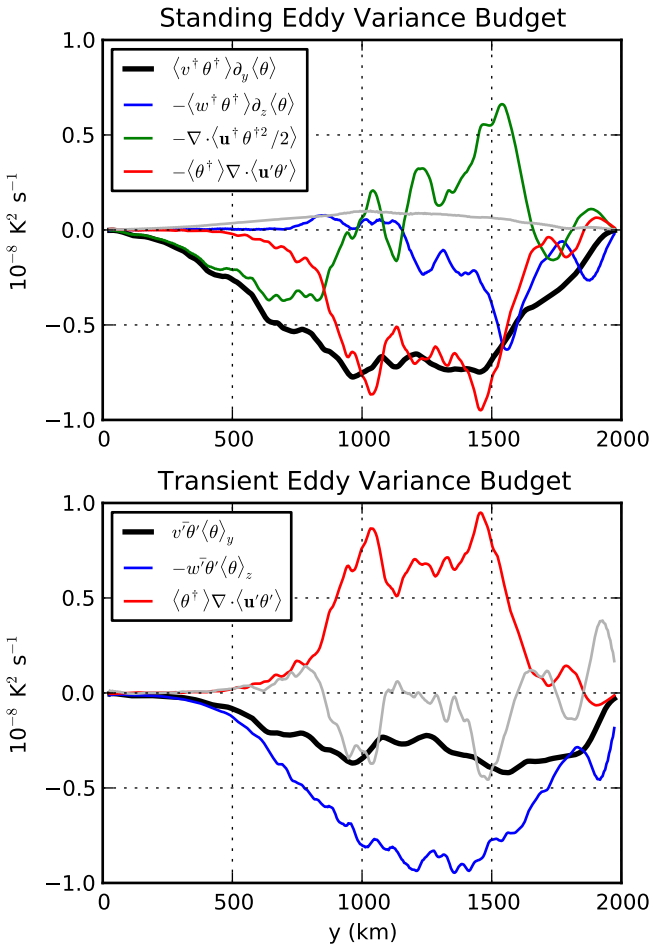

FIG. 6. Vertical average of the dominant terms in the standing eddy (17) and transient eddy (18) variance budgets . The light gray line is the residual of the plotted terms.

5. Heat Transport Across Streamlines

It has long been recognized that the importance of standing eddies is greatly reduced by adopting a coordinate system which follows the meanders of the ACC. One such coordinate system was proposed by de Szoeke and Levine (1981), who analyzed the heat transport across a contour of depth-averaged potential temperature. (We will

call this quantity Θ.) While this coordinate is not precisely a streamline of the ACC, the Θ contours are certainly much more aligned with the ACC streamlines than are latitude circles. By analyzing a hydrographic atlas of the Southern Ocean, de Szoeke and Levine (1981) found that the time-mean geostrophic flow transports no heat across a Θ-contour within the ACC. They inferred that transient eddy heat transport was required to close the heat budget. This conclusions was later confirmed by performing the same analysis in numerical models, where the transient eddy flux was known (**?**).

The idea of "streamwise" coordinates was taken up from the perspective of the momentum budget by Marshall et al. (1993). They noted that, in an isopycnal coordinate system, the standing eddy component of the interfacial form stress (related to the meridional heat transport) could be eliminated completely by averaging along time-mean contours of the Montgomery potential in each isopycnal layer. Transient eddy interfacial form stress was therefore required to close the momentum budget. Such an analysis was performed by **?** and **?** in idealized models; they both found that the transient eddy flux across Montgomery-potential contours was highly localized in regions downstream of topographic features. The notion that standing eddies can be removed by a coordinate transformation became a cornerstone of the residual-mean model of the ACC, which should be interpreted as a mean along streamlines (Karsten and Marshall 2002; Marshall and Radko 2003; Olbers et al. 2004; Olbers and Visbeck 2005). But these theoretical models were strongly influenced by laboratory and numerical experiments without topography, in which a zonal and streamwise average are indistinguishable (Karsten et al. 2002; Marshall et al. 2002; Cenedese et al. 2004; Kuo et al. 2005). One shortcoming of this analogy is that truly zonally symmetric models have uniform eddy statistics in x, while models with topography can have strong local hotspots of cross-stream eddy flux (Thompson 2010). (This is precisely what we find below.)

Most recently, Viebahn and Eden (2012) examined how to best construct the meridional overturning streamfunction using both along-isopycnal and along-streamline integration paths. The goal of this analysis was to eliminate completely the standing-eddy contribution to the MOC, which is directly related to both the heat transport and the interfacial form stress. They found that the standing-eddy component could only be eliminated completely by using a streamwise coordinate which varied with depth (similar to the conclusion by Marshall et al. 1993); since such a coordinate system would be non-orthogonal, this transformation comes at the expense of great geometrical complexity. Viebahn and Eden (2012) conclude that a streamwise coordinate which does not vary with depth (like that of de Szoeke and Levine 1981) is adequate to remove most of the standing-eddy component.

One goal of streamwise averaging is to make the meandering ACC as close as possible to a zonally symmetric flow. The conceptual advantages of this transformation for simple theoretical models are clear. But our experiments have shown that a zonally symmetric channel with the exact same forcing is different in important ways from one with topography. In the previous sections, we have attributed this difference to the presence of heat transport by the standing eddies. But how can the difference be explained when the standing eddies have been eliminated through averaging along streamlines?

a. Streamwise Coordinate Systems

The time-mean heat transport across any closed contour S_0 of $S(x,y)$ can be expressed as

$$\mathcal{H}^{S_0} = \rho_0 c_p \oint_{S_0} \left(\int_{-H}^{0} \overline{\boldsymbol{v}\theta} dz \right) \cdot \hat{\boldsymbol{n}}_S dS \tag{19}$$

$$= \rho_0 c_p \int\int_{S<S_0} \nabla \cdot \left(\int_{-H}^{0} \overline{\boldsymbol{v}\theta} dz \right) dx dy \tag{20}$$

where $\hat{\boldsymbol{n}}_S = \nabla S / |\nabla S|$ is the unit normal vector to S. The overbar indicates a time average, as in the preceding sections. In the second line, we have used the divergence theorem, yielding an expression that is much easier to evaluate in practice from a numerical model. For our case, we tested two different streamwise coordinate systems. The first is defined by Θ, identically to de Szoeke and Levine (1981). The other uses the barotropic transport streamfunction Ψ. These two quantities are given by

$$\Theta(x,y) = \frac{1}{H} \int_{-H}^{0} \overline{\theta} dz$$

$$\Psi(x,y) = -\int_{0}^{y} \int_{-H}^{0} \overline{v} dz dy' \ . \tag{21}$$

S can be either Θ or Ψ. In what follows, we refer to both these contours as "streamlines," although Θ is clearly not a streamfunction. As we will see, the results of our analysis using these two coordinates are similar in most ways. The two fields are plotted in Fig. 7. The isolines of both Θ and Ψ are primarily zonal away from the ridge but they meander coherently above and downstream of the ridge. These meanders arise due to the standing-wave dynamics discussed in the preceding sections. An important qualitative *difference* between Ψ and Θ is that Ψ contains regions of closed contours that do not circumnavigate the domain (for example, the regions where $\Psi < -15$ Sv or $\Psi > 75$ Sv). The transport across these contours can no longer be interpreted as across the circumpolar current; rather, it is across the boundary of a barotropic gyre-like recirculation. On the other hand, there are certain Θ contours that are not closed at all, but intersect the northern boundary ($\Theta > 1.6°$C). Aside from these problematic regions, the

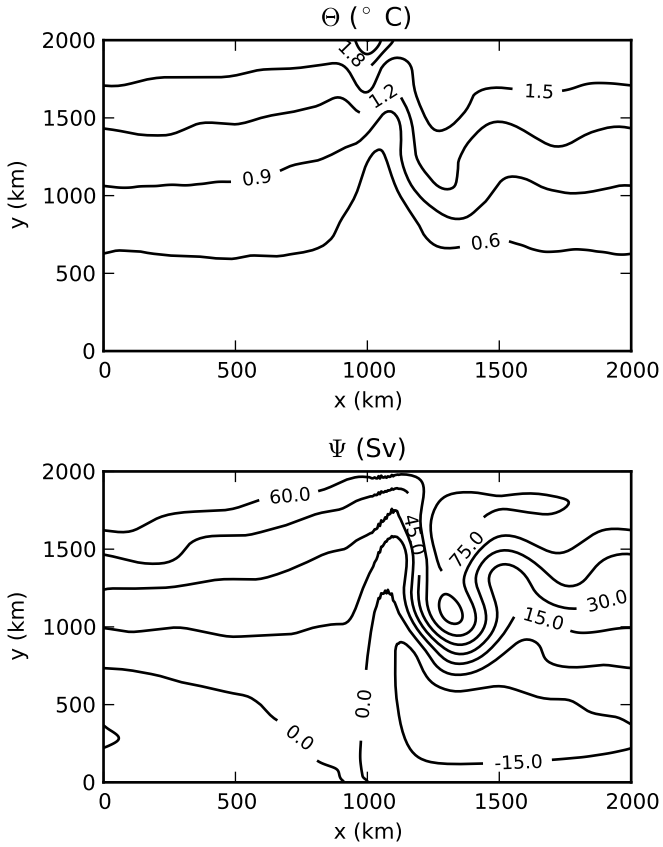

FIG. 7. The two streamwise coordinates Ψ and Θ, defined according to (21), for the reference ridge experiment ($\tau_0 = 0.2$ N m^{-2}).

contours of both quantities are well-behaved over most of the domain, accurately representing the meandering front.

To isolate the physical processes governing the cross-stream heat transport, we separate the term $\overline{\boldsymbol{v}\theta}$ into ageostrophic (i.e. Ekman), standing eddy, and transient eddy components as follows:

$$\overline{\boldsymbol{v}\theta} = \overline{\boldsymbol{v}}_a\overline{\theta} + \overline{\boldsymbol{v}}_g\overline{\theta} + \overline{\boldsymbol{v}'\theta'} \tag{22}$$

where $\boldsymbol{v}_a$ and $\boldsymbol{v}_g$ are the ageostrophic and geostrophic components of the time-mean flow. The second term is the standing eddy flux and the third is the transient eddy flux (which is predominantly geostrophic). By decomposing the flux in this way, we can separately diagnose $\mathcal{H}^S_{Ek}$ (the ageostrophic, Ekman driven heat transport), $\mathcal{H}^S_g$ (the total geostrophic flow heat transport), $\mathcal{H}^S_{SE}$ (the standing-eddy component of $\mathcal{H}^S_g$), and $\mathcal{H}^S_{TE}$ (the transient-eddy component) using (20), analogously to the meridional heat transport components defined in Sec. 4. The difference is that these fluxes are across streamlines defined by S, rather than latitude circles. (By choosing $S = y$, we could recover the standard meridional heat transport definition.)

We examine these different components of the heat flux across Θ contours in Fig. 4 for the reference simulations. These plots are in the same figure as the meridional heat transport from the previous section to facilitate comparison. They are also plotted as a function of Y_{eq} the "equivalent latitude" of the Θ contour to further facilitate comparison. We see that the overall magnitude of the cross-stream heat flux by the Ekman transport is similar in both coordinates, peaking around 100 TW. This heat transport is balanced by a geostrophic flux, leading to very small net $\mathcal{H}^\Theta$. By decomposing $\mathcal{H}^\Theta_g$, the poleward heat transport by the geostrophic motions, into standing and transient components, we see that in *the standing eddy heat flux is indeed very close to zero*, and the transient eddies are what balance the Ekman-induced heat flux. This is in strong contrast to Fig. 4, where standing eddies dominated the flux across latitude circles.

The picture given by Ψ coordinates is nearly identical and is not shown. The main difference is that the transports across Ψ contours do not display the secondary peaks near the northern boundary which are evident in $\mathcal{H}^\Theta_{Ek}$ and $\mathcal{H}^\Theta_{SE}$. We note that these peaks merely indicate a repartitioning of a weak heat transport into two compensating components. This peak is associated with Θ contours that intersect the boundary and is therefore somewhat spurious; the Ψ contours cannot intersect the boundary and display no such behavior. Nevertheless, we prefer Θ contours for our subsequent analysis because they do not contain local extrema.

We now examine how the balance depends on wind stress. Components of the cross-Θ heat transport are plotted as a function of τ_0 in Fig. 5 for both flat and ridge experiments, again side-by-side with the meridional heat transport analysis from the previous section. (The equivalent results for Ψ are nearly identical and are not shown.) The increasing winds drive more and more heat across the Θ contours via the Ekman transport, with the same depend one τ_0 seen using zonal averaging. But in contrast from the zonal averages, the standing eddy component $\mathcal{H}^\Theta_{SE}$ remains rather small. Instead, as in the flat-bottomed experiments, the transient eddy heat flux is what primarily balances $\mathcal{H}^\Theta_{Ek}$ in the ridge case, accounting about 90% of the total $\mathcal{H}^\Theta_g$.

The initial impression given by the streamwise analysis is in line the perspective advanced by Marshall and Radko (2003) and Olbers and Visbeck (2005): that adopting a streamwise coordinate renders the system with topography seemingly isomorphic to the zonally symmetric case with no topography, wherein the dominant balance is between Ekman advection and transient eddy fluxes. However, there are at least two important differences: with a ridge the eddy heat transport is more efficient, as demonstrated by the smaller h, and thus less available potential

energy present in the system. Another difference is that the eddy heat flux itself is not distributed uniformly along a streamwise contour, as in the flat-bottom case—instead it is highly localized downstream of the ridge. To properly explore this, we must look at the local eddy heat flux in the (x, y) plane.

b. Local Cross-Stream Heat Flux

We now analyze the structure of $\overline{\boldsymbol{v}\theta} \cdot \hat{\boldsymbol{n}}$ locally, to see where heat is fluxed across streamlines. In the flat-bottom case, the eddy statistics are largely homogeneous in the x-direction, so that the cross-stream heat fluxes (Ekman and transient eddy) are spread evenly along a streamline. Prior studies of idealized circumpolar currents with topographic ridges (**??**) have shown that eddy thickness fluxes (related to the PV flux) are concentrated in regions near and downstream of the topographic ridge. A similar conclusion was reached by **?** in an analysis of altimetric data; they found that Lagrangian trajectories cross the ACC fronts preferentially in a few locations downstream of major topographic features such as Drake Passage or Kerguelen plateau. Therefore, it is not surprising that our eddy heat flux is similarly localized.

To illustrate the localization of the heat flux we show the *divergent* part of $\overline{\boldsymbol{v}\theta}$, which, from (20), is the only component contributing to the cross-stream heat flux. Yet locally, the eddy flux can be dominated by a rotational component, obscuring the physics of cross-stream transport (Marshall and Shutts 1981; **?**; **?**; **?**). In our numerical model, we can isolate the divergent part by solving the elliptic Poisson problem

$$\nabla^2 \phi(x, y) = \nabla \cdot \left(\int_{-H}^{0} \overline{\boldsymbol{v}\theta} dz \right) \tag{23}$$

subject to the Neumann boundary condition that $\phi_x = 0$ at the northern and southern boundaries. The divergent component of the temperature flux is then given by

$$\boldsymbol{F}^{div}(x, y) = \nabla \phi \ . \tag{24}$$

We solve (23) for ϕ numerically using an algebraic multigrid solver.[2] We also solve separately for the steady ageostrophic, geostrophic, and transient eddy components of the divergence, giving three separate fields $\boldsymbol{F}_a^{div}$, $\boldsymbol{F}_g^{div}$ and $\boldsymbol{F}_{TE}^{div}$. Dotted with $\hat{\boldsymbol{n}}$, these three components correspond to $\mathcal{H}_{Ek}^{\Theta}$, $\mathcal{H}_{SE}^{\Theta}$, and $\mathcal{H}_{TE}^{\Theta}$, the three components of the cross-stream heat transport identified above.

We plot the the vertically integrated divergent eddy temperature flux in Fig. 8 as arrows in the (x, y) plane, separated into a time mean (both geostrophic and ageostrophic) and transient eddy component. This figure also shows the magnitude of the the flux normal to $\nabla\Theta$. It is striking how the divergent flux is aligned perpendicular to the Θ contours, meaning that ϕ and Θ are themselves aligned. This means that the eddy fluxes "know" about Θ and that it is a naturally choice of streamwise coordinate. (Recall that the method for identifying the divergent portion of the flux is completely unrelated to the choice of streamwise coordinates.)

The eddy flux is nearly entirely down-gradient, as expected since it is just the divergent part (Marshall and Shutts 1981). The cross-stream flux occurs mostly in the vicinity of the strong meander downstream of the ridge. In fact, close inspection of the arrows in Fig. 8 reveals that $\boldsymbol{F}_{TE}^{div}$ is mostly a *zonal* flux across the Θ contours running north-south. These zonal fluxes go in both direction out and away from the trough of the standing wave. No wonder the transient eddies did not make a strong contribution to the meridional heat transport! The most important eddy heat fluxes are actually zonal, not meridional at all.

The steady flux is equal and opposite to the eddy flux. It is clear that this must be due to the combined action of ageostrophic and geostophic flus. The Ekman flux is spread broadly over the domain (not shown), so the steady geostrophic responds by advecting heat back and forth across Θ contours in such a way as to bring about the pattern seen in the figure. While contributing little to the integrated cross-stream heat flux, $\overline{\boldsymbol{v}}_g\overline{\theta}$ therefore plays an important role in organizing the zonal structure of the total steady cross-stream flux (left panel of Fig. 8).

From this divergent eddy heat flux, it is possible to construct a local cross-stream eddy diffusivity. We define this diffusivity as

$$K_{\perp}^{div}(x, y) = -\frac{1}{H} \frac{\boldsymbol{F}_{TE}^{div} \cdot \hat{\boldsymbol{n}}}{|\nabla\Theta|} \tag{25}$$

where H is the full depth.This quantity measures the local efficiency of eddies at transporting heat across the Θ contours. $K_{\perp}^{div}$ is plotted in Fig. 9, for both the flat and ridge reference experiments. For the flat-bottom experiment, $K_{\perp}^{div}$ is zonally uniform, peaking in the northern part of the domain around 4000 m^2 s^{-1}. For the ridge experiments, $K_{\perp}^{div}$ is highly variable in space. The region of highest diffusivity is downstream of the ridge in the standing meander, particularly on the right side of the wave trough. In this region, diffusivities exceed 5000 m^2 s^{-1}. This region is precisely where the gradients are also strongest, leading to an extremely strong local cross-stream flux. In the western part of the domain, but the diffusivity and the gradient are weak. This local correlation between strong mixing and strong gradient is perhaps the greatest challenge for constructing a theoretical model based only on streamwise-averaged quantities. We will return to this point in the forthcoming discussion.

[2]This python-based solver is freely available at `https://code.google.com/p/pyamg/`.

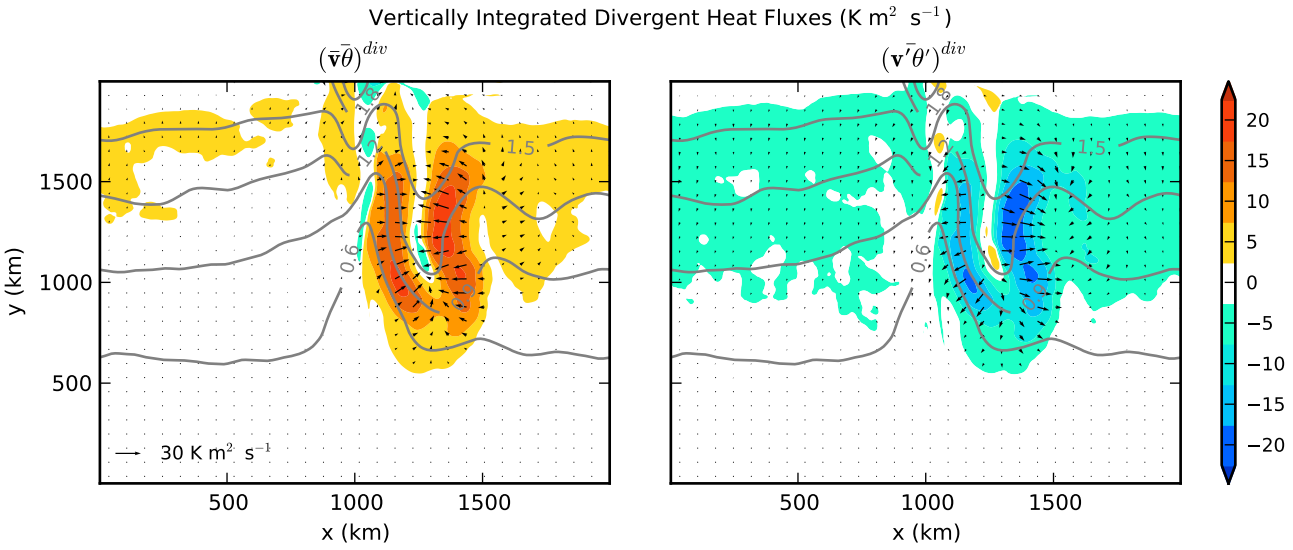

FIG. 8. *Top Row:* Components of the heat transport across Θ contours in the x, y plane.

6. Local versus global eddy growth

The localization of the eddy fluxes just downstream of the ridge should be constrasted with their diffuse presence in the flat bottom case (cf. the two panels of figure 9). This qualitative difference is associated with fundamentally different propagating properties of the eddies. This is illustrated in figure 11, which shows the surface vorticity at $y = 1250$ km as a function of x and t: with the flat bottom (top panel) eddies propagate at a speed which is intermediate between the surface zonally averaged velocity (dashed black line) and the vertically and zonally averaged velocity (black solid line); with the ridge (lower panel), the eddies are almost stationary, moving eastward at a speed no larger than the vertically and zonally averaged velocity (black solid line) and much smaller than the surface velocity (dashed black line). Because there is a weak eastward eddy propagation, the maximum eddy activity is downstream of the ridge (**?**).

This difference in propagation indicates that in the flat case the eddies are generated and maintained through convective (or global) instability, while with the ridge eddies are generated and maintained through absolute (or local) instability (**??**). With topography, the generation of a standing meander localized the horizontal buoyancy gradients in the vicinity of the ridge (cf. the gray isotherms in figure 8), providing a local source of available potential energy which eddies can release. An additional requirement for local growth is that the mean flow is slow enough to keep the eddies in place as they grow. The ridge reduces the speed of the zonal flow by reducing its barotropic component relative to the flat case. Indeed, the barotropic flow, as measured by U_0, is much smaller with the ridge than without it, because of the fundamentally different momentum budget with and without topograhpy (cf. the bottom left panel of figure ???). With the ridge, mean buoyancy gradients are locally enhanced and eddies propagate more slowly: the net result is a higher efficiency at extracting energy from the mean flow. The difference in absolute versus convective instability is especially apparent in the initial transient development (**is there a figure that we can show?**). As the eddies equilibrate in the ridge case, there is an additional positive feedback which enhances their growth: as eddies transport heat northward, they restratify the interior, reducing the vertical extent of the zonal shear and thus the baroclinic component of the mean eastward zonal flow, proportional to h. This process further slows down the mean flow, allowing continued extraction of mean flow energy by the eddies.

7. Discussion and Conclusions

[[I have started writing this section, but it is incomplete. Need to discuss more to decide what to emphasize.]]

We have examined the equilibration of idealized circumpolar currents with and without topography. The point of this exercise was to reach a deeper understanding of how the thermocline depth is determined. In our simplified problem, the thermocline depth is regulated completely by the efficiency of the geostrophic flow at transporting heat poleward. The amount of heat transported must approxi-

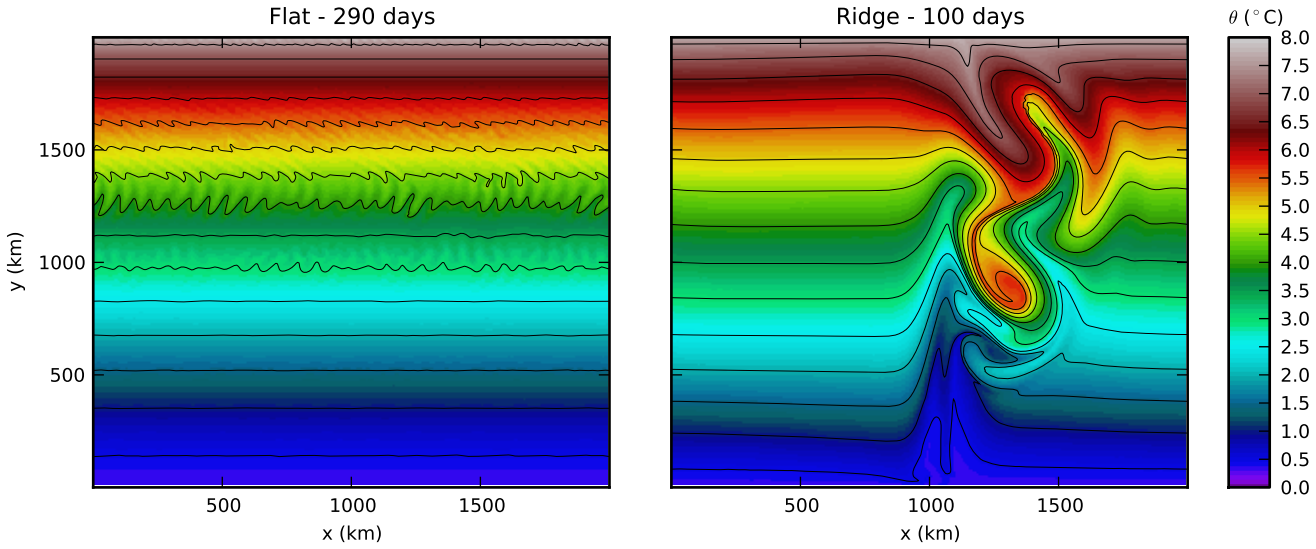

FIG. 10. Spinup of surface θ. Shows initial instability growth.

mately balance the equatorward heat transport by the Ekman circulation; the thickness of the layer over which the heat is returned poleward is the thermocline depth. A more efficient geostrophic heat transport can accomplish the necessary heat transport in a shallower layer.

We first analyzed the simulations using a standard zonal-averaged framework. From this perspective, the chief difference between the simulations with topography is that they contain both standing and transient eddies, while the flat-bottomed case contains only transient eddies. For the same forcing, the thermocline depth is significantly shallower when topography is present. Furthermore, the sensitivity of the thermocline depth to the wind stress is less when topography is present, indicating a more complete state of eddy saturation. In the experiments with topography, the geostrophic meridional heat transport is strongly dominated by the standing eddy contribution. Therefore, from this zonally averaged perspective, the eddy saturation phenomenon is properly understood as an equilibration between wind-driven Ekman fluxes and standing eddy fluxes. This should be kept in mind when analyzing more realistic models, where standing eddies play a similarly prominent role.

We also analyzed the heat transport across the the meandering front using two different "streamwise" coordinates, one based on the depth-averaged temperature (Θ) and one based on the barotropic transport streamfunction (Ψ).

Our study suggests that we have been framing the equilibration problem incorrectly. All of the current theoretical models for the ACC stratification rely on eddy diffusivity closures based on zonally or streamwise-averaged fields alone, i.e. a fundamentally axisymmetric background state (Johnson and Bryden 1989; Karsten et al. 2002; Cessi and Fantini 2004; Marshall and Radko 2003; Olbers and Visbeck 2005; Cessi 2008; Jansen and Ferrari 2012; Nikurashin and Vallis 2012). Many of these models can trace their closure schemes back to the two-layer quasigeostrophic equilibration problem studied by Held and Larichev (1996), or to the diffusive closures made by Green (1970) and Stone (1972) in an atmospheric context. (See also **?**Schneider 2006, for a review of the atmospheric side of the problem.) Ultimately, these theories are finite-amplitude, nonlinear closures of the classic baroclinic instability problems posed by Charney (1947), Eady (1949), and Phillips (1951) for zonally-symmetric background states.

A powerful criticism of this paradigm can be found in **?**, who examined the baroclinic instability of a simple flow with variations of the shear in the zonal direction. Such a problem is clearly applicable to our model, and indeed to the real ACC. There are important qualitative differences between this "local" instability problem and the classical zonally symmetric problem, such as a strong dependence on the barotropic zonal mean flow. (The zonally symmetric problem is essentially gallilean-invariant and is therefore insensitive to the addition of a barotropic mean zonal flow, but this invariance is broken by the addition of fixed topography.) The unstable local modes are confined spatially to the region downstream of the maximum shear.

The strong spatial variation in mixing along a Θ con-

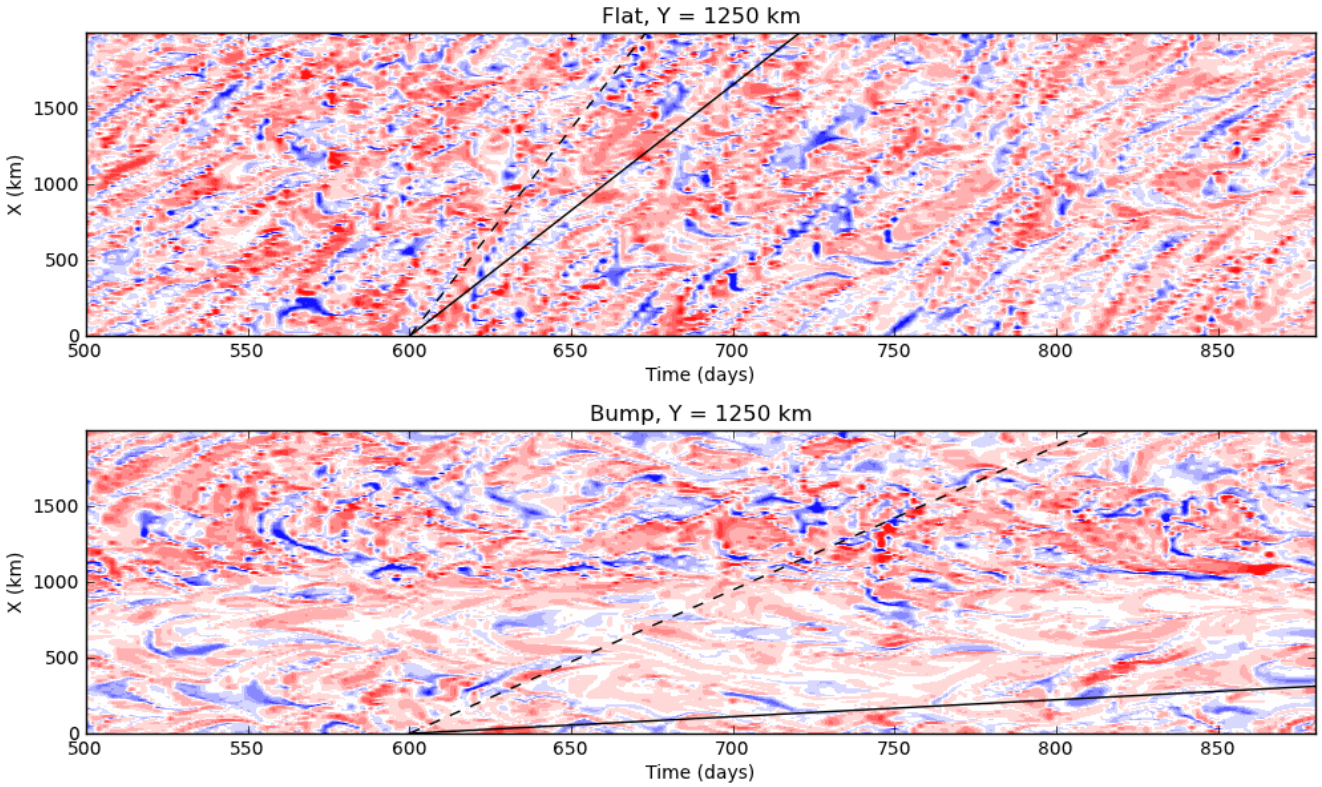

FIG. 11. Hovmoeller diagram of vorticity. The dashed line indicates the surface zonal velocity and the solid line the barotropic zonal velocity.

tour means that a diffusive closure for the cross-stream transient eddy heat flux based on the *streamwise-averaged* background gradient is unlikely to be satisfactory. To see this more clearly we can rewrite the cross-stream eddy heat transport using the diffusivity defined in (25) as

$$\mathcal{H}^{\Theta}_{TE} = \rho_0 c_p \oint_{\Theta} \boldsymbol{F}^{div}_{TE} \cdot \hat{\boldsymbol{n}} ds = -\rho_0 c_p \oint_{\Theta} K^{div}_{\perp} |\nabla\Theta| ds \ . \quad (26)$$

If $K^{div}_{\perp}$ were approximately constant along the contour, it could be removed from the integral, and $\mathcal{H}^{\Theta}_{TE}$ could be written only in terms of this constant and the streamwise-averaged $|\nabla\Theta|$. But in fact, Fig. 9 shows that $K^{div}_{\perp}$ and $|\nabla\Theta|$ are strongly correlated in space, with large diffusivity precisely where the gradients are strong.

Acknowledgments.

Start acknowledgments here.

APPENDIX

Is there one?

I don't know.

REFERENCES

Abernathey, R., J. Marshall, and D. Ferreira, 2011: The dependence of southern ocean meridional overturning on wind stress. *J. Phys. Oceanogr.*, **41 (12)**, 2261–2278.

Cenedese, C., J. Marshall, and J. A. Whitehead, 2004: A laboratory model of thermocline depth and exchange fluxes across circumpolar fronts. *J. Phys. Oceanogr.*, **34**, 656–668.

Cessi, P., 2007: Regimes of thermocline scaling: The interaction of wind stress and surface buoyancy. *J. Phys. Oceanogr.*, **37**, 2009–2021.

Cessi, P., 2008: An energy-constrained parameterization of eddy buoyancy flux. *J. Phys. Oceanogr.*, **38**, 1807–1820.

Cessi, P. and M. Fantini, 2004: The eddy-driven thermocline. *J. Phys. Oceanogr.*, **34**, 2642–2659.

Charney, J. G., 1947: The dynamics of long waves in a baroclinic westerly current. *J. Meteor.*, **4**, 135–162.

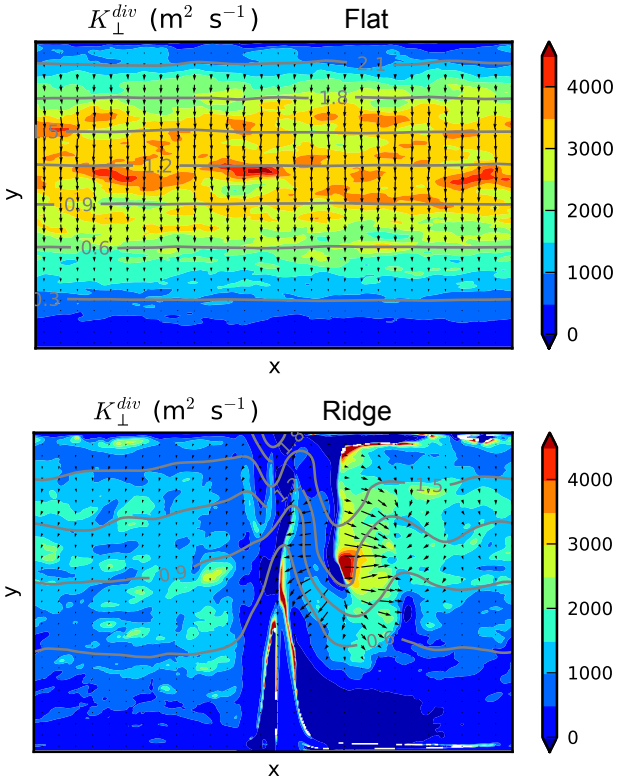

FIG. 9. Local eddy diffusivity for the vertically-integrated divergent eddy heat flux, defined according to (25). The Θ contours are shown in gray. The direction and magnitude of the divergent eddy heat flux $\boldsymbol{F}_{TE}^{div}$ are indicated by the black arrows. The integrated flux across contours is essentially the same in both experiments.

de Szoeke, R. A. and M. D. Levine, 1981: The advective flux of heat by mean geostrophic motions in the southern ocean. *Deep Sea Res.*, **28A (10)**, 1057–1085.

Dufour, C. O., J. Le Sommer, J. D. Zika, M. Gehlen, J. C. Orr, P. Mathiot, and B. Barnier, 2012: Standing and transient eddies in the response of the Southern Ocean meridional overturning to the Southern Annular Mode. *J. Climate*, **25**, 6958–6974.

Eady, E., 1949: Long waves and cyclone waves. *Tellus*, **1**, 33–52.

Farneti, R., T. L. Delworth, A. J. Rosati, S. M. Griffies, and F. Zeng, 2010: The role of mesoscale eddies in the rectification of the southern ocean response to climate change. *J. Phys. Oceanogr.*, **40**, 1539–1558.

Gent, P. and J. McWilliams, 1990: Isopycnal mixing in ocean circulation models. *J. Phys. Oceanogr.*, **20**, 150–155.

Green, J. S. A., 1970: Transfer properties of the large-scale eddies and the general circulation of the atmosphere. *Quart. J. Roy. Meteor. Soc.*, **96**, 157–185.

Hallberg, R. and A. Gnanadesikan, 2006: The role of eddies in determining the structure and response of the wind-driven southern hemisphere overturning: Results from the modeling eddies in the souther ocean (meso) project. *J. Phys. Oceanogr.*, **36**, 2232–2252.

Haney, R. L., 1971: Surface thermal boundary condition for ocean circulation models. *J. Phys. Oceanogr.*, **1**, 241–248.

Held, I. M. and V. D. Larichev, 1996: A scaling theory for horizontally homogeneous, baroclinically unstable flow on a beta plane. *J. Atmos. Sci.*, **53 (7)**, 946–953.

Hill, C., D. Ferreira, J.-M. Campin, J. Marshall, R. Abernathey, and N. Barrier, 2012: Controlling spurios diapycnal mixing in eddy-resolving height-coordinate ocean models: Insights from virtual deliberate tracer release experiments. *Ocean Modelling*, **45-46**, 14–26.

Hughes, C. W., 1997: Comments on on the obscurantist physics of 'form drag' in theorizing about the circumpolar current. *J. Phys. Oceanogr.*, **27**, 209–210.

Jansen, M. and R. Ferrari, 2012: Macroturbulent equilibration in a thermally forced primitive equation system. *J. Atmos. Sci.*

Johnson, G. C. and H. L. Bryden, 1989: On the size of the Antarctic Circumpolar Current. *Deep Sea Res.*, **36**, 39–53.

Karoly, D. J., P. C. McIntosh, P. Berrisford, T. J. McDougall, and A. C. Hirst, 1997: Similarities of the deacon cell in the southern ocean and ferrel cells in the atmosphere cells in the atmosphere. *Q. J. R. Meteorol. Soc.*, **123**, 519–526.

Karsten, R., H. Jones, and J. Marshall, 2002: The role of eddy transfer in setting the stratification and transport of a circumpolar current. *J. Phys. Oceanogr.*, **32**, 39–54.

Karsten, R. and J. Marshall, 2002: Constructing the residual circulation of the acc from observations. *J. Phys. Oceanogr.*, **32**, 3315–3272.

Kuo, A., R. A. Plumb, and J. Marshall, 2005: Transformed eulerian-mean theory. part ii: Potential vorticity homogenization and equilibrium of a wind- and buoyancy-driven zonal flow. *J. Phys. Oceanogr.*, **45**, 175–187.

Large, W. G., J. C. McWilliams, and S. C. Doney, 1994: Oceanic vertical mixing: A review and a model with a nonlocal boundary layer parameterization. *Reviews of Geophysics*, **32 (4)**, 363–403.

Lee, M.-M. and A. Coward, 2003: Eddy mass transport for the Southern Ocean in an eddy-permitting global ocean model. *Ocean Modeling*, **5**, 249–266.

Marshall, G., 2003: Trends in the southern annular mode from observations and reanalyses. *J. Climate*, **16**, 4134–4144.

Marshall, J., A. Adcroft, C. Hill, L. Perelman, and C. Heisey, 1997a: A finite-volume, incompressible navier stokes model for studies of the ocean on parallel computers. *J. Geophys. Res.*, **102**, 5753–5766.

Marshall, J., C. Hill, L. Perelman, and A. Adcroft, 1997b: Hydrostatic, quasi-hystrostatic, and non-hydrostatic ocean modeling. *J. Geophys. Res.*, **102**, 5733–5752.

Marshall, J., H. Jones, R. Karsten, and R. Wardle, 2002: Can eddies set ocean stratification? *J. Phys. Oceanogr.*, **32**, 26–38.

Marshall, J., D. Olbers, H. Ross, and D. Wolf-Gladrow, 1993: Potential vorticity constraints on the dynamics and hydrography of the southern ocean. *J. Phys. Oceanogr.*, **23**, 465–487.

Marshall, J. and T. Radko, 2003: Residual mean solutions for the antarctic circumpolar current and its associated overturning circulation. *J. Phys. Oceanogr.*, **33**, 2341–2354.

Marshall, J. and G. Shutts, 1981: A note on rotational and divergent eddy fluxes. *J. Phys. Oceanogr.*, **21**, 1677–1681.

Meredith, M. P. and A. M. Hogg, 2006: Circumpolar response of southern ocean eddy activity to a change in the southern annular mode. *Geophys. Res. Lett.*, **33**, L16 608.

Meredith, M. P., A. C. Naveira Garabato, A. M. Hogg, and R. Farneti, 2012: Sensitivity of the overturning circulation in the southern ocean to decadal changes in wind forcing. *J. Phys. Oceanogr.*, **42**, 99–110.

Morrison, A. K. and A. M. Hogg, 2012: On the relationship between Southern Ocean overturning and acc transport. *J. Phys. Oceanogr.*

Munday, D., H. L. Johnson, and D. P. Marshall, 2012: Eddy saturation of equilibrated circumpolar currents. *J. Phys. Oceanogr.*

Nikurashin, M. and G. Vallis, 2012: A theory of the interhemispheric meridional overturning circulation and associated stratification. *J. Phys. Oceanogr.*

Olbers, D., 1998: Comments on "on the obscurantist physics of 'form drag' in theorizing about the circumpolar current". *J. Phys. Oceanogr.*, **28**, 1647–1655.

Olbers, D., D. Borowski, C. Voelker, and J. Wolff, 2004: The dynamical balance, transport and circulation of the antarctic circumpolar current. *Antarctic Science*, **16**, 439–470.

Olbers, D. and V. O. Ivchenko, 2001: On the meridional circulation and balance of momentum in the southern ocean of pop. *Ocean Dynamics*, **52**, 79–93.

Olbers, D. and M. Visbeck, 2005: A model of the zonally averaged stratification and overtuning in the souther ocean. *J. Phys. Oceanogr.*, **35**, 1190–1206.

Phillips, N. A., 1951: A simple three-dimensional model for the study of large-scale extratropical flow paterns. *J. Meteorology*, **8 (381-393)**.

Prather, M. J., 1986: Numerical advection by conservation of second-order moments. *J. Geophys. Res.*, **91 (D6)**, 6671–6681.

Schneider, T., 2006: The general circulation of the atmosphere. *Annu. Rev. Earth Planet. Sci.*, **34**, 655–88.

Speer, K., S. Rintoul, and B. Sloyan, 2000: The diabatic deacon cell. *J. Phys. Oceanogr.*, **30**, 3212–3223.

Spence, P., O. A. Saenko, M. Eby, and A. J. Weaver, 2009: The southern ocean overturning: Parameterized versus permitted eddies. *J. Phys. Oceanogr.*, **39**, 1634–1652.

Stone, P. H., 1972: A simplified radiative-dynamical model for the static stability of rotating atmospheres. *J. Atmos. Sci.*, **29 (3)**, 405–417.

Straub, D., 1993: On the transport and angular momentum balance of channel models of the antarctic circumpolar current. *J. Phys. Oceanogr.*, **23 (776-783)**.

Thompson, A. F., 2010: Jet formation and evolution in baroclinic turbulence with simple topography. *J. Phys. Oceanogr.*, **40**, 257–274.

Toggweiler, J. R., 2009: Shifting westerlies. *Science*, **232**, 1434–1435.

Toggweiler, R. and J. Russell, 2008: Ocean circulation in a warming climate. *Nature*, **451**, 286–288.

Toggweiler, R. and B. Samuels, 1995: Effect of Drake Passage on the global thermohaline circulation. *Deep Sea Res. I*, **42 (4)**, 477–500.

Viebahn, J. and C. Eden, 2010: Toward the impact of eddies on the response of the southern ocean to climate change. *Ocean Modelling*, **34**, 150–165.

Viebahn, J. and C. Eden, 2012: Standing eddies in the meridional overturning circulation. *J. Phys. Oceanogr.*, **42**, 1486–1508.

Wolfe, C. and P. Cessi, 2011: The adiabatic pole-to-pole overturning circulation. *J. Phys. Oceanogr.*, **41**, 1795–1810.

Wolfe, C. L. and P. Cessi, 2010: What sets the strength of the mid-depth stratification and overturning circulation in eddying ocean models? *J. Phys. Oceanogr.*, **40**, 1520–1538.